Journal of Autonomous Intelligence (2024) Volume 7 Issue 5
doi: 10.32629/jai.v7i5.921

ORIGINAL RESEARCH ARTICLE

Model-based hybrid variational level set method applied to lung cancer detection

Wang Jing[1], Liew Siau Chuin[1,*], Azian Abd Aziz[2]

[1] *Faculty of Computing, Universiti Malaysia Pahang, Pekan 96100, Pahang, Malaysia*

[2] *Kulliyyah of Medicine, International Islamic University Malaysia, Kuantan 25100, Malaysia*

*** Corresponding author:** Liew Siau Chuin, liewsc@ump.edu.my

ABSTRACT

The precise segmentation of lung lesions in computed tomography (CT) scans holds paramount importance for lung cancer research, offering invaluable information for clinical diagnosis and treatment. Nevertheless, achieving efficient detection and segmentation with acceptable accuracy proves to be challenging due to the heterogeneity of lung nodules. This paper presents a novel model-based hybrid variational level set method (VLSM) tailored for lung cancer detection. Initially, the VLSM introduces a scale-adaptive fast level-set image segmentation algorithm to address the inefficiency of low gray scale image segmentation. This algorithm simplifies the (Local Intensity Clustering) LIC model and devises a new energy functional based on the region-based pressure function. The improved multi-scale mean filter approximates the image's offset field, effectively reducing gray-scale inhomogeneity and eliminating the influence of scale parameter selection on segmentation. Experimental results demonstrate that the proposed VLSM algorithm accurately segments images with both gray-scale inhomogeneity and noise, showcasing robustness against various noise types. This enhanced algorithm proves advantageous for addressing real-world image segmentation problems and nodules detection challenges.

Keywords: lung cancer; medical image; computed tomography

ARTICLE INFO

Received: 25 July 2023
Accepted: 1 August 2023
Available online: 12 March 2024

1. Introduction

In 2020, the global incidence of lung cancer is about 11.4%, and the mortality rate is 18%, which has become the leading cause of death from malignant tumors[1]. In the classification of lung cancer, non-small cell lung cancer (NSCLC) accounts for about 85% of the total number of lung cancer[2]. For the diagnosis of lung cancer, pathology-related examinations are still the gold standard; however, tumor biopsy is an invasive procedure, and patients cannot obtain tumor tissue due to the high risk of obtaining tissue. In addition, tumors are heterogeneous in time and space, and the information on tumor tissue obtained at a certain site and at a certain time period cannot fully represent the information of the tumor.

Currently, imaging techniques and pathological examinations are mainly used to screen lung cancer, but imaging techniques are expensive and have poor specificity, and pathological examinations are invasive[3]. As the disease progresses, it is often accompanied by infection and severe pain in the late stage, which seriously affects the health and quality of life of patients[4,5]. At present, pathological biopsy is still the gold standard for its diagnosis. Since the disease has not been specifically manifested in the early stage, most patients have

progressed to the middle and late stage when diagnosed, which adversely affects the treatment effect[6]. Therefore, finding specific detection indicators has become a hot spot in clinical practice. The tumor markers are substances synthesized and released by tumor cells, which have the advantages of simple collection and less trauma, and have many applications in early diagnosis, disease progression and prognosis assessment of tumor diseases[7]. Therefore, the heterogeneity between tumors and within tumors brings challenges to guide clinical decision-making. Based on this, liquid biopsy is currently attracting attention because of its advantages of non-invasiveness, rapidity, and real-time application, and a series of studies on it are in progress. Liquid biopsy refers to the collection of non-solid biological tissues such as blood samples to detect biomarkers, improve tumor molecular typing, and provide relevant information for the Equation of treatment plans.

This study presents MODEL-BASED hybrid variational level set method (VLSM) tailored for lung cancer detection. Brief a comprehensive review of leave-set detection techniques for pulmonary nodules in computerized-tomography (CT) images. The primary objectives are to assess the latest technologies employed in developing computational diagnostic tools for biomedical data acquisition, storage, processing, and analysis. Additionally, the research evaluates progress made, existing challenges, and future prospects in this domain.

2. Related works

Most lung cancers are prone to metastases, and when they are first detected they are already at an advanced stage, making them difficult to cure. Therefore, early screening for lung cancer can significantly improve survival rates. Tissue imaging techniques remain the mainstay of lung cancer screening, including chest X-rays, CT (computed tomography), MRI (magnetic resonance imaging), and PET (positron emission tomography)[7–10].

2.1. Chest X-ray

A chest x-ray produces images of the inside of the chest by using very small doses of ionizing radiation[11]. It is used to evaluate lung, heart, and chest wall function and to help diagnose symptoms such as shortness of breath, persistent cough, fever, chest pain, or injury. It can also be used to help diagnose and monitor various lung diseases such as pneumonia, emphysema and lung cancer. Because chest X-ray examination is quick and easy, it is widely used in emergency diagnosis and treatment[12]. However, chest x-rays do not give a definitive diagnosis and often cannot distinguish cancer from other conditions such as lung abscesses (collections of pus that form in the lungs). Lung cancer is often at an advanced stage by the time a tumor is detected on a chest x-ray[13].

2.2. Computed Tomography (CT)

Computed tomography (CT) is usually done after a chest x-ray in screening for disease. A CT scan uses X-rays and a computer to create detailed images of the inside of the body (**Figure 1**)[14]. Low-dose helical computed tomography (LDCT) detects almost six times more nodules than conventional X-rays, research shows. LDCT has a resolution of less than 1 cm and the ability to produce a three-dimensional view of the lungs, making it a high-quality alternative to X-rays. However, the high sensitivity of LDCT also produces a higher false positive rate than traditional mammography, with false positive rates ranging from 20% to 50%. To date, there are still no authoritative studies that clearly identify LDCT as the best lung cancer screening tool[10,13].

2.3. Positron emission tomography (PET)

Positron emission tomography (PET) is a nuclear medicine functional imaging technique used to observe metabolic processes in vivo to aid in the diagnosis of diseases[8]. Over the past few decades, positron emission tomography (PET), with its ability to provide functional data using the glucose analog 18F-fluorodeoxyglucose (FDG), has evolved from a primary research tool to a fundamental imaging tool for the assessment of lung

cancer. Preferential uptake of 18F-FDG into tumor cells produces a high tumor-to-background intensity ratio, which facilitates the detection of tumor foci and the cellular characterization of tumor cells[15]. Despite its high sensitivity for malignancy detection, PET often cannot be used as a single imaging modality in clinical practice due to its limited spatial resolution. Taken together, PET and CT technologies are often combined into a dual-purpose unit called PET-CT. By providing anatomical and metabolic information, PET-CT scanners can provide better results when diagnosing or staging cancer (**Figure 2**). In addition, PET-CT scans can show the location of active cancer cells, and cancer cells before structural changes develop. This method helps identify tumors so that we can properly diagnose and stage the disease and focus treatment on the cancerous tissue. However, exposure to radiation during a PET-CT scan may increase the risk of future cancer in healthy individuals[16].

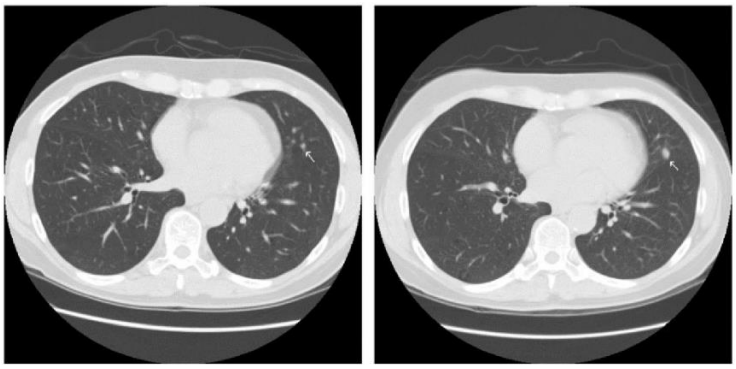

Figure 1. CT scan image of the lungs[15].

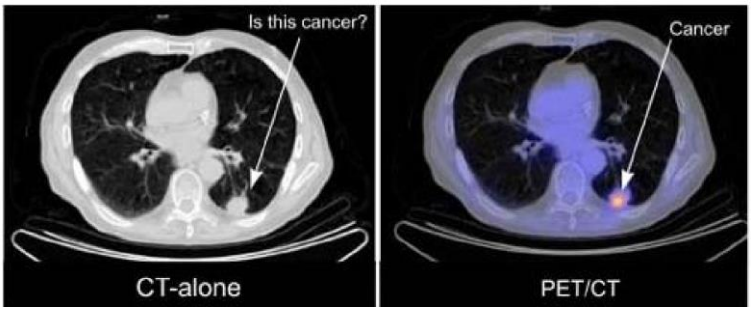

Figure 2. CT (left) and PET-CT (right) scan images of the lungs[17].

2.4. Magnetic resonance imaging (MRI)

Magnetic resonance imaging (MRI) is a medical imaging technique used in radiology to create images of anatomy (**Figure 3**). MRI scanners use strong magnetic fields, magnetic field gradients, and radio waves to generate images of internal organs[16]. MRI does not involve X-rays or ionizing radiation, unlike CT and PET scans. A special dye called a contrast agent is given before the scan to produce a clearer image. The dye can be injected into a patient's vein or given as a pill or liquid. MRI scans are not good at taking pictures of moving body parts, and the lungs move with breathing. Therefore, this method is rarely used in the observation of lung cancer[17]. However, it may be helpful in finding lung cancer that has spread to the brain or bones. Although MRI is not currently considered a primary imaging modality for early diagnosis and staging of lung cancer, it has some advantages over other imaging modalities, suggesting that the use of this method with other techniques should be expanded[10,18,19].

3. Proposed method

The previous part discusses the segmentation method of uneven grayscale images, and does not pay attention to the effect of noise on segmentation. In reality, images are often interfered by noise during the process of acquisition and transmission, which seriously reduces image quality. The segmentation method

based on offset correction level set usually uses Euclidean distance to construct data items, but the noise robustness of this measurement method is poor. For an image with gray unevenness and noise at the same time, the local grayscale changes in each target area are caused by the gray unevenness and noise. In this way, the local image variance cannot be used to measure the degree of gray-scale unevenness of the image. The adaptive scale operator proposed by the pervious part will be invalid, affecting the estimation of the offset field and reducing the segmentation accuracy of the gray-scale uneven image.

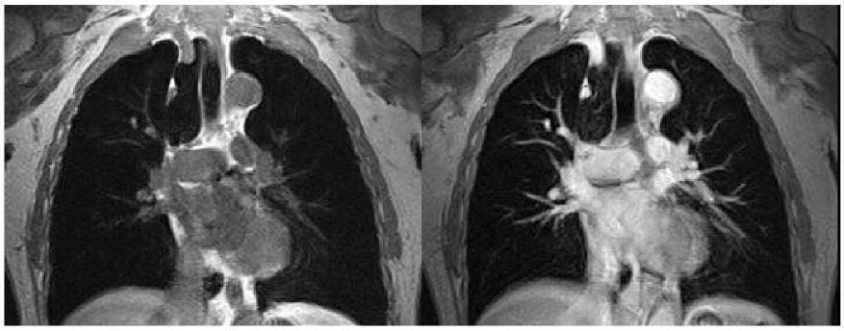

Figure 3. MRI scan image of the lungs[18].

As a solution to the issues mentioned above, this technique suggests using a hybrid level-setting method that is based on kernel metric (KMHLS). First, an enhanced multi-scale mean filter is put to use in order to make an estimate of the picture's offset field. Then, an offset correction is applied to the image in order to lessen the gray level inhomogeneity that the image has. After that, the kernel measurement technique is used to construct energy items using local and global information in the appropriate proportions. As an additional measure, the local similarity measurement approach has been included in the energy term in order to reduce the impact of noise. In order to develop a hybrid energy function, a new weight function is used to adaptively alter the weight coefficients of the two different energy components. In conclusion, the count gradient regularization term is implemented in order to further lessen the impact that noise has. After first being provided in the form of a two-phase level-set segmentation, the suggested method for segmentation is later modified to support several phases of the process.

3.1. Kernel measurement

The offset correction level set method based on K-means clustering usually uses Euclidean distance to construct data items, but this measurement method lacks robustness to noise and outliers, and severely reduces the segmentation accuracy of noisy images. Therefore, the L_2 norm can be replaced by a non-linear distance metric. Usually, the kernel method is used for nonlinear distance measurement. The commonly used kernel function can be expressed as (Wu et al.[20]):

$$K(\boldsymbol{a},\boldsymbol{b}) = \langle \varphi(\boldsymbol{a}), \varphi(\boldsymbol{b}) \rangle = \varphi(\boldsymbol{a})^T \varphi(\boldsymbol{b}) \tag{1}$$

among them, $\boldsymbol{a}$ and $\boldsymbol{b}$ are vectors with the same dimension, $\varphi(.)$ represents the non-linear mapping from the original data space to the feature space, $\langle .,. \rangle$ represents the inner product operation, and T represents the transpose operation.

The Gaussian radial basis function is a commonly used kernel function[21], expressed as:

$$K(a,b) = exp\left(-\frac{(a-b)^2}{\sigma}\right) \tag{2}$$

among them, the parameter σ represents the bandwidth of the kernel function, and $K(a,a) = 1$. Then, the non-Euclidean distance metric in the feature space is expressed as (Wu et al.[18]):

$$\| \varphi(a) - \varphi(b) \|^2 = \big(\varphi(a) - \varphi(b)\big)^T \varphi(a) - \varphi(b) = K(a,a) + K(b,b) - 2K(a,b) = 2 - 2K(a,b) \tag{3}$$

3.2. Hybrid Level Set Segmentation Algorithm

This section first uses an improved multi-scale mean filter to estimate the offset field of the image to reduce the gray-scale unevenness of the image. Then, the kernel metric and local similarity metric are used to suppress the influence of noise. Finally, the count gradient regularization term is used to further reduce the influence of noise.

3.3. Improved Multi-Scale Mean Filter

The MSF model[22] uses a multi-scale mean filter to estimate the offset field of the gray inhomogeneous image. However, this model uses a fixed number of scales. For some small-sized images, a larger scale will cause the offset field to be excessively smooth, and the local grayscale change information of the image cannot be obtained, leading to incorrect segmentation. Therefore, this thesis proposes an improved multi-scale mean filter, which can approximate the offset field of the image and obtain more local variation information of the offset field.

The higher the degree of unevenness of the gray level of the image, the more severe the local gray level changes in the smooth area of the image. Therefore, try to use small-scale mean filtering to estimate the offset field of the image to obtain more local change information, which is beneficial to remove the serious grayscale inhomogeneity of the image, and only retains the slight grayscale inhomogeneity. The scale number k of the multi-scale mean filter is defined as:

$$k = \min\left(round\left(\sqrt{N_0/(4\pi)}\right), k_{max}\right) \tag{4}$$

among them, N_0 is the number of pixels of the image I, and k_{max} is a positive integer, which represents the maximum number of scales of the multi-scale mean filter.

In this way, the i scale parameter of the multi-scale mean filter is expressed as:

$$r_i = i, i = 1,2,\cdots,k \tag{5}$$

In addition, by weighting the image gray level to reduce the influence of salt and pepper noise and singular values, the mean filter with a scale of r_i is defined as:

$$AF_i(x) = \frac{\sum_{y\in R_{x,i}} I(y)\cdot w(y)}{\sum_{y\in R_{x,i}} w(y)} \tag{6}$$

among them, $R_{x,y} = \{y: |y-x| \le r_i\}$ represents a partial circular area with x as the center and radius r_i. $w(\cdot)$ is the weight function of image gray level, defined as:

$$AF_i(x) = \frac{\sum_{y\in R_{x,i}} I(y)\cdot w(y)}{\sum_{y\in R_{x,i}} w(y)} \tag{7}$$

among them, $*$ is a convolution operator, K_0 is a normalized mean filter with a size of $(2w_0+1)\times(2w_0+1)$, and σ_0 is:

$$\sigma_0 = \left(\frac{1}{N_0-1}\sum_{j=1}^{N_0}(d(x_j)-\bar{d})^2\right)^{0.5} \tag{8}$$

among them, $d(x) = |I(x)-\bar{I}|$, $\bar{I}$ represents the average gray value of image I, and $\bar{d}$ represents the average value of $d(x)$.

Then, the approximate estimation of the offset field of the uneven grayscale image is:

$$B_0(x) = \frac{1}{k}\sum_{i=1}^{k} AF_i(x)\Big/\bar{I} \tag{9}$$

according to the uneven gray scale image model, through offset correction, the image I_1 after offset correction is obtained as:

$$I_1(x) = \frac{I(x)}{B_0(x)}, x \in \Omega \tag{10}$$

The improved multi-scale averaging filter can well eliminate the unevenness of slightly uneven grayscale images, while for severely uneven grayscale images, it can greatly reduce the unevenness, leaving only slight grayscale unevenness. At the same time, the filter has strong robustness to noise.

3.4. Energy functional

The image I_I after the offset correction generally has slight grayscale unevenness. The (local intensity clustering Mumford-Shah) LIC-CV model[21] can segment images with slight gray unevenness quickly, accurately and robustly. Therefore, this thesis uses the LIC-CV model to construct the energy functional, and can use fixed scale parameters. The kernel function estimates the offset field and eliminates the influence of scale parameters on the segmentation of uneven grayscale images. At the same time, this thesis introduces the kernel metric method into the LIC-CV model, and replaces the Euclidean distance metric in the energy functional with the kernel metric to improve the robustness to noise. In this way, the energy term based on local area information is expressed as:

$$E^{local}(\phi, b, c) = \sum_{i=1}^{N} \lambda_i \int \big(1 - K_L(I_1, b, c_i)\big) M_i\big(\phi(x)\big) dx \tag{11}$$

among them, $M_i(\phi)$ is the membership function, and $K_L(I_I, b, c_i)$ is defined as the form of the kernel metric:

$$K_L(I_1, b, c_i) = \exp\left(-\int K_\sigma\,(y - x)((I_1(x) - b(y)c_i)^2/\sigma_1) dy\right) \tag{12}$$

among them, σ_I can be obtained by using image I_I and Equation (5–8), $k_\sigma(\cdot)$ is a Gaussian kernel function with a standard deviation of σ.

The energy item based on the global area information is:

$$E^{global}(\phi, c^{cv}) = \sum_{i=1}^{N} \lambda_i \int \big(1 - K_G(I_1, c_i^{cv})\big) M_i\big(\phi(x)\big) dx \tag{13}$$

among them, $K_G(I_I, c_i^{cv})$ is defined as the form of nuclear metric:

$$K_G(I_1, c_i^{cv}) = \exp\left(-\frac{(I_1(x) - c_i^{cv})^2}{\sigma_1}\right) \tag{14}$$

Secondly, considering the spatial relationship between the center pixel and its neighborhood, this method uses the local block similarity[23] to further reduce the impact of noise, and the local and global energy terms can be converted into:

$$K_G(I_1, c_i^{cv}) = \exp\left(-\frac{(I_1(x) - c_i^{cv})^2}{\sigma_1}\right) \tag{15}$$

$$E^{global}(\phi, c^{cv}) = \int \sum_{i=1}^{N} \lambda_i \int Z(|z - x|)\big(1 - K_G(I_1, c_i^{cv})\big) M_i\big(\phi(x)\big) dx dz \tag{16}$$

among them, the kernel function $Z(\cdot)$ is defined as:

$$Z(u) = \begin{cases} \frac{1}{2}\exp\left(-\frac{u^2}{h}\right), |u| \le r \\ 0, \quad other \end{cases} \tag{17}$$

among them, h is the bandwidth and r is the scale parameter.

In addition, this thesis suggests a novel weight function as a means of dynamically modifying the relative importance of regional and international energy variables. The weight of the global energy item is automatically adjusted according to the degree of gray-level unevenness of the image, whereas the weight of the local energy item is automatically adjusted according to the gray-level uniformity of the image. This is

because the global energy item can only handle the gray-level uniform image, whereas the local energy item can handle the gray-level uneven image. The gray-level unevenness of the picture may be described using the offset field b, as stated by the gray-level uneven image model[21]. The offset field value of the gray-level uniform image is 1, and the farther b deviates from 1, the image The more significant the unevenness in the gray scale. Hence, a new weight function is constructed by making use of the estimated offset field while the algorithm is going through the iteration process:

$$\omega(x) = vexp(-l(b(x)-1)^2) \tag{18}$$

among them, v and l are constant parameters.

v For the two-phase segmentation, that is, N = 2, this thesis uses a binary step function to represent the inner and outer regions of the evolution curve C, which is defined as:

$$\phi(x) = \begin{cases} -1, x \in inside(C) \\ 1, x \in outside(C) \end{cases} \tag{19}$$

Then the membership function of each subregion is expressed as: $M_1(\phi(x)) = (1+\phi(x))/2$ and $M_2(\phi(x)) = (1-\phi(x))/2$. Using the weight function in Equation (16) to combine the local and global energy terms, the mixed energy function is obtained as:

$$\begin{aligned} E^H(\phi, b, c, c^{cv}) = &\int \sum_{i=1}^{2} \lambda_i \int (1-\omega(x)) Z(|z-x|)\big(1-K_L(I_1, b, c_i)\big) M_i\big(\phi(x)\big) dx\, dz \\ &+ \int \sum_{i=1}^{2} \lambda_i \int \omega(x) Z(|z-x|)\big(1-K_G(I_1, c_i^{cv})\big) M_i\big(\phi(x)\big) dx dz \end{aligned} \tag{20}$$

In addition, this thesis introduce the length term and rule term[23] based on L_0 regularization to regularize the level set function to ensure the stability of the level set evolution and further suppress the influence of noise. A weighted Regional Scale Variable Fitting (RSF) model that is based on local entropy has been established at the top in order to increase the original model's robustness with respect to the beginning contour position and considerable noise. This is a very important development. In fact, owing to the heterogeneity of the gray scale, the difference in gray scale across various places in a picture that has an uneven distribution of gray is often varied. This is because a picture with an uneven distribution of gray contains a picture that has an uneven distribution of gray. A new local fitting energy function is proposed to replace the existing ones in the CV and Local Binary Fitting (LBF) models, with the aim of addressing intensity inhomogeneity more effectively. The proposed energy function takes into consideration the advantages and disadvantages of the CV and RSF models. This new approach is expected to improve the ability to handle intensity inhomogeneity in image analysis. The Therefore benefits of the proposed method will be a more accurate and robust image segmentation and analysis process:

$$E^{CER} = \gamma E^H(\phi, b, c, c^{cv}) + \mu C(\nabla\phi) + \nu C(\phi + 1) \tag{21}$$

among them, γ, μ and ν are constant parameters, $C(\cdot)$ represents the L_0 counting operator, and $C(\phi+1)$ represents the number of pixels satisfying $|\phi + 1| \neq 0$.

3.5. Level set evolution and numerical realization

By minimizing the energy function in Equation (21), image segmentation can be achieved and the offset field can be estimated at the same time. Using the alternate iterative minimization method to solve, the energy functional E is minimized relative to each variable in the Equation (21), and the closed solution of each variable M can be obtained:

$$c_i = \frac{\int (b * K) I_1 M_i(\phi) W_i^L dx}{\int (b^2 * K) M_i(\phi) W_i^L dx}, i = 1, \cdots, N \tag{22}$$

$$b = \frac{(I_1 J^{(1)}) * K}{J^{(2)} * K} \tag{23}$$

$$= \frac{\int I_1(x) M_i(\phi(x)) W_i^G dx}{\int M_i(\phi(x)) W_i^G dx}, i = 1, \cdots, N. and\ x \in \Omega \tag{24}$$

among them, $J^{(1)} = \sum_{i=1}^{N} W_i^L c_1 M_i(\phi)$, $J^{(2)} = \sum_{i=1}^{N} W_i^L {c_1}^2 M_i(\phi)$, $W_i^L = \exp(-(I_1 - bc_1)^2/\sigma_1)$, $W_i^G = \exp(-(I_1 - c_i^{cv})^2/\sigma_1)$.

When c_i, b and c_i^{cv} are fixed, the relative level set function ϕ minimizes the energy function. However, two counting operators are introduced in the mixed energy functional, namely $C(\nabla\phi)$ and $C(\phi + 1)$, which cannot be solved directly by the gradient descent method. To this end, auxiliary variables are introduced, and the level set function is evolved using the alternate iteration optimal method[23]. Similar to the LODL model, the mixed energy function is discretized, and three auxiliary variables φ, ξ and ψ are introduced for $\partial_x\phi_p, \partial_y\phi_p$ and ϕ respectively, the final discrete energy functional can be obtained as:

$$\begin{aligned} E = \gamma E^H(\phi, b, c, c^{cv}) + \mu C(\varphi, \xi) + \nu C(\psi) + \alpha \sum_p ((\partial_x\phi_p - \phi_p)^2 + (\partial_y\phi_p - \xi_p)^2) \\ + \beta \sum_p (\phi_p + 1 - \psi_p)^2 \end{aligned} \tag{25}$$

among them, $C(\varphi, \xi) = \{p: |\phi_p| + |\xi_p| \neq 0\}, C(\psi) = \{p: |\psi_p| \neq 0\}$, $\alpha > 0$ and $\beta > 0$ as a parameter, α needs to be adjusted according to the image. Replace $C(\varphi, \xi)$and $C(\psi)$ with $\sum_p B(|\phi_p| + |\xi_p|), \sum_p B(\psi_p)$, where $B(x)$ is a binary function, if $x \neq 0$, then its value is 1, otherwise it is 0. Therefore, the final discrete energy functional is:

$$\begin{aligned} E = \gamma E^H(\phi, b, c, c^{cv}) + \mu \sum_p B(|\phi_p| + |\xi_p|) + \nu \sum_p B(\psi_p) + \alpha \sum_p ((\partial_x\phi_p - \phi_p)^2 \\ + (\partial_y\phi_p - \xi_p)^2) + \beta \sum_p (\phi_p + 1 - \psi_p)^2 \end{aligned} \tag{26}$$

Using the alternate iterative optimization method, (φ, ξ) and ψ can be obtained as:

$$(\varphi_p, \xi_p) = \begin{cases} (0,0), & (\partial_x\phi_p)^2 + (\partial_y\phi_p)^2 \leq \mu/\alpha \\ (\partial_x\phi_p, \partial_y\phi_p), & (\partial_x\phi_p)^2 + (\partial_y\phi_p)^2 > \mu/\alpha \end{cases} \tag{27}$$

$$\psi_p = \begin{cases} 0, (\phi_p + 1)^2 \leq \nu/\beta \\ \phi_p + 1, (\phi_p + 1)^2 > \nu/\beta \end{cases} \tag{28}$$

For the level set function ϕ, the corresponding Euler equation can be obtained:

$$\begin{aligned} 2(\beta\phi - \alpha\nabla\phi) = \frac{1}{2}\gamma \cdot Z \\ * \left(-\lambda_1\left(2 - (1-\omega)K_L(I_1, b, c_1) - \omega K_G(I_1, c_1^{cv})\right)\right. \\ \left. + \lambda_2\left(2 - (1-\omega)K_L(I_1, b, c_2) - \omega K_G(I_1, c_2^{cv})\right)\right) + 2\beta(\psi - 1) + 2\alpha(\partial_x^*\varphi + \partial_y^*\xi) \end{aligned} \tag{29}$$

among them, ∂_x^* and ∂_y^* represent the complex conjugate of ∂_x and ∂_y, respectively.

Using Fast Fourier Transform (FFT) to solve the Equation (19)[23], this thesis can get:

$$\phi_0 = F^{-1}\left[\frac{F(Q) + 2\alpha\left(F(\partial_x^*)F(\varphi) + F(\partial_y^*)F(\xi)\right)}{2\beta + 2\alpha\left(F^*(\partial_x)F(\partial_x) + F^*(\partial_y)F(\partial_y)\right)}\right] \tag{30}$$

among them, $F(\cdot)$ represents the Fourier transform, $F^{-1}(\cdot)$ is the inverse Fourier transform, F^* represents the complex conjugate of F, and Q is defined as:

$$\begin{aligned} Q = \frac{1}{2}\gamma \cdot Z * \left(-\lambda_1\left(2 - (1-\omega)K_L(I_1, b, c_1) - \omega K_G(I_1, c_1^{cv})\right)\right. \\ \left. + \lambda_2\left(2 - (1-\omega)K_L(I_1, b, c_2) - \omega K_G(I_1, c_2^{cv})\right)\right) + 2\beta(\psi - 1) \end{aligned} \tag{31}$$

Finally, a Gaussian filter with a scale of σ_s is used to smooth the level set function ϕ_0 and perform

binarization processing $\phi_0(x)$:

$$\phi(x) = \begin{cases} 1, \phi_0(x) \geq 0 \\ -1, \phi_0(x) < 0 \end{cases} \tag{32}$$

In the numerical implementation (Appendix B), in order to maintain the stability of the evolution of the level set function, the gray level of the original image I_1 is linearly compressed to the interval [0,1]. And the level set functionϕ_0 that is not regularized into a binary function is used to calculate c_i, b and c_i^{cv}, where the membership function is expressed as $M_1(\phi_0(x)) = H(\phi_0(x))$ and $M_2(\phi_0(x)) = 1 - H(\phi_0(x))$, the Heaviside function $H(\phi)$ is defined as:

$$H_\varepsilon(\phi) = \frac{1}{2}\left[1 + \frac{2}{\pi} \cdot \arctan(\frac{\phi}{\varepsilon})\right] \tag{33}$$

among them, ε is a constant parameter.

The initial constants c_i^{cv} and c_i can be calculated by the following Equation:

$$c_1^{cv} = c_1 = \frac{\int I_1(1+\phi)dx}{\int(1+\phi)dx}, c_2^{cv} = c_2 = \frac{\int I_1(1-\phi)dx}{\int(1-\phi)dx}, x \in \Omega \tag{34}$$

The main steps of the proposed hybrid level set binary segmentation algorithm (VLSM) based on kernel metric are as follows:

Step 1. Calculate B_0 according to Equation (4), and obtain the image I_1 after offset correction according to Equation (5);

Step 2. Initialize the offset field $b_0(x) = 1, x \in \Omega$, initialize ϕ^0, c_i^{cv} and c_i according to the Equation (14) and Equation (19), and according to the Equation (3) Calculate σ_1;

Step 3. According to Equation (17), Equation (18) and Equation (19) respectively calculate c_i, b and c_i^{cv};

Step 4. Calculate $(\varphi, \xi)$and ψ according to Equation (22) and Equation (23);

Step 5. Obtain the level set functionϕ_0 according to Equation (25);

Step 6. Obtain the binary level set functionϕ according to Equation (27);

Step 7. When the maximum number of iterations is reached or the level set function converges, the algorithm ends, otherwise, return to step 3.

3.6. Multiphase level set

The two-phase segmentation form is extended to the polyphase form. When N = 3, two level set functions ϕ_1 and ϕ_2 are used to define different target areas in the image domain Ω, and the polyphase, b, mixed function can be obtained:

$$\begin{aligned} E_M^H(\Phi, b, c, c^{cv}) = &\int \sum_{i=1}^{3} \lambda_i \int \big(1 - \omega(x)\big) Z(|z-x|)(1 - K_L(I_1, b, c_i)) M_i(\Phi) dx dz \\ &+ \int \sum_{i=1}^{3} \lambda_i \int \omega(x) Z(|z-x|)(1 - K_G(I_1, c_i^{cv})) M_i(\Phi) dx dz \end{aligned} \tag{35}$$

among them, $M_1(\Phi) = (1+\phi_1)(1+\phi_2)/4$, $M_2(\Phi) = (1+\phi_1)(1-\phi_2)/4$ and $M_3(\Phi) = (1-\phi_1)/2$ represents membership function $\Phi = (\phi_1, \phi_2)$.

The final multiphase energy functional is defined as:

$$E_M(\Phi, b, c, c^{cv}) = \gamma E_M^H(\Phi, b, c, c^{cv}) + \mu C(\nabla\phi_1) + \nu C(\phi_1 + 1) + \mu C(\nabla\phi_2) + \nu C(\phi_2 + 1) \tag{36}$$

The level set function ϕ_1 can be obtained by Equations (25) and (27), where Q is defined as:

$$Q = \frac{1}{2}\gamma \cdot Z * \big(-\lambda_1\big(2-(1-\omega)K_L(I_1,b,c_1)-\omega K_G(I_1,c_1^{cv})\big)(1+\phi_2)/2 - \lambda_2\big(2-(1-\omega)K_L(I_1,b,c_2)-\omega K_G(I_1,c_2^{cv})\big)(1-\phi_2)/2\big) + \lambda_3\big(2-(1-\omega)K_L(I_1,b,c_2)-\omega K_G(I_1,c_2^{cv})\big)) + 2\beta(\psi_1-1) \quad (37)$$

among them, (φ_1, ξ_1) and ψ_1 can be obtained according to Equation (22) and Equation (23) respectively.

Similarly, the level set function ϕ_2 is obtained by Equation (25) and Equation (27), where Q is defined as:

$$Q = \frac{1}{2}\gamma \cdot Z * \big(-\lambda_1\big(2-(1-\omega)K_L(I_1,b,c_1)-\omega K_G(I_1,c_1^{cv})\big)(1+\phi_1)/2 + \lambda_2\big(2-(1-\omega)K_L(I_1,b,c_2)-\omega K_G(I_1,c_2^{cv})\big)(1+\phi_1)/2\big) + 2\beta(\psi_2-1) \quad (38)$$

where, (φ_2, ξ_2) and ψ_2 are obtained according to Equation (22) and Equation (23) respectively.

4. Result and discussion

After excluding the 399 examples, the dataset contains 4384 nodule annotations that were labeled consistently. However, in order to further eliminate uncertain circumstances, the total number of annotations used was reduced to 2817.

Figures 4 and **5** present a summary of patient demographic and scan information, collected by reviewing the DICOM file data from the LIDC dataset. Among the 734 scans, there is no available information about the subject's age or gender. However, among the remaining 284 instances that have gender information (DICOM Tag ID: 0010, 0040) available, there is a distribution of 49.3% males and 50.7% females. Additionally, when age information (DICOM Tag ID: 0010, 1010) is provided, as shown in **Figure 4**, the median age is 61 years old. It's worth noting that this value may be considered a place holder for the tag. Importantly, there are no instances where information about a person's age is known without also knowing their gender.

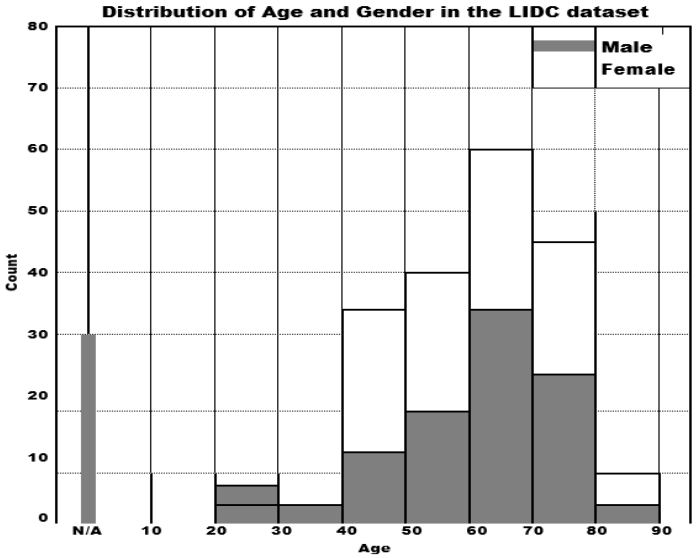

Figure 4. Distribution of age and sex in the LIDC dataset.

Figure 4 presents an illustration of the pixel spacing distribution within a slice of the scan (DICOM Tag ID: 0028, 0030) and the thickness of each slice (DICOM Tag ID: 0018, 0050), both measured in millimeters. The median pixel spacing is found to be 0.7 mm, while the median slice thickness of the CT scan image volumes is 2 mm. The distributions of scanner resolutions in the LIDC dataset are depicted in **Figure 5**. The left side displays the distribution of pixel spacing within the slice, with a median of 0.7 mm. On the right side, the distribution of slice thickness for CT scan image volumes is shown, revealing a median value of 2 mm or

less.

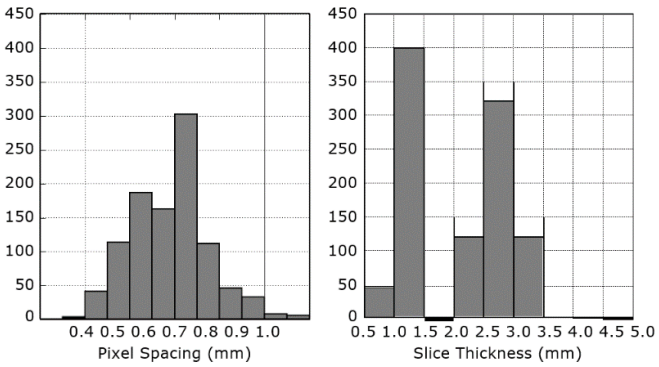

Figure 5. Sample related to pixel spacing and slice thickness.

The information provided here is derived from a scoring system ranging from 1 to 5 was used to assess the presence of a certain trait in **Figure 6**. A score of 1 indicated a low presence of the trait, while a score of 5 indicated a strong presence as shown in **Figure 5**. The level of agreement among four individuals who annotated a nodule as belonging to a specific type of structure determined the number of annotations assigned to each nodule. The total annotations for a given nodule could vary from one to four. Identifying which annotations referred to the same physical nodule in a scan proved challenging due to the lack of a universally unique identifier for the physical nodules among the various annotations.

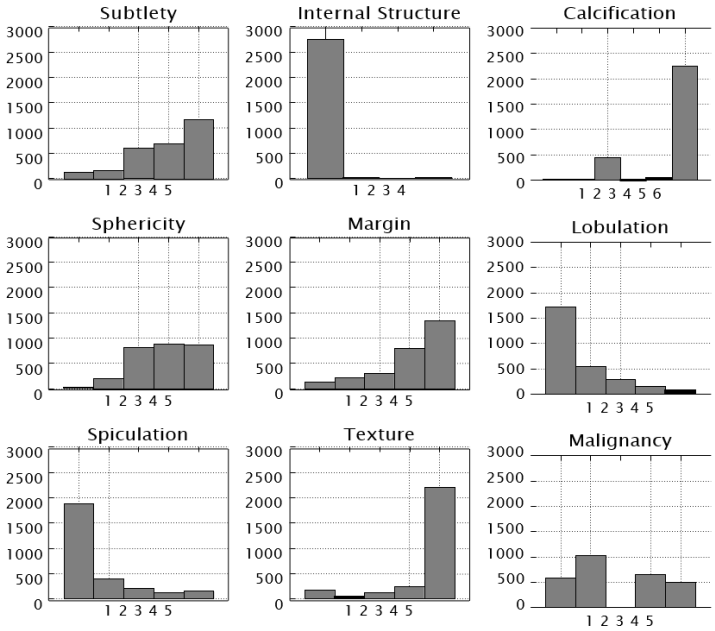

Figure 6. Distribution of annotation values for image features and malignancy. Note the excluded bin for the indeterminate malignancy value of 3.

Figure 7 displays the center (17th) slice through the image volume of each of the 20 lung nodules in the testing dataset. The red curve in the figure represents the contour from the slice, obtained through the ground-truth segmentation surface. On the other hand, the blue curve represents the contour from the slice, acquired through the approximate segmentation surface using the proposed method with the zero level set. The results depicted in **Figure 7** demonstrate the effectiveness of the proposed method across various contexts. This includes successful segmentation of juxta-pleural nodules (e.g., **Figure 7(14,15)**), nodules with cavities (e.g., **Figure 7(11,12)**), non-solid nodules (e.g., **Figure 7(8)**), and irregularly-shaped nodules (e.g., **Figure 7(20)**). These visual observations, coupled with the previously mentioned quantitative results, affirm the success of the proposed approach in lung nodule image segmentation within CT image volumes.

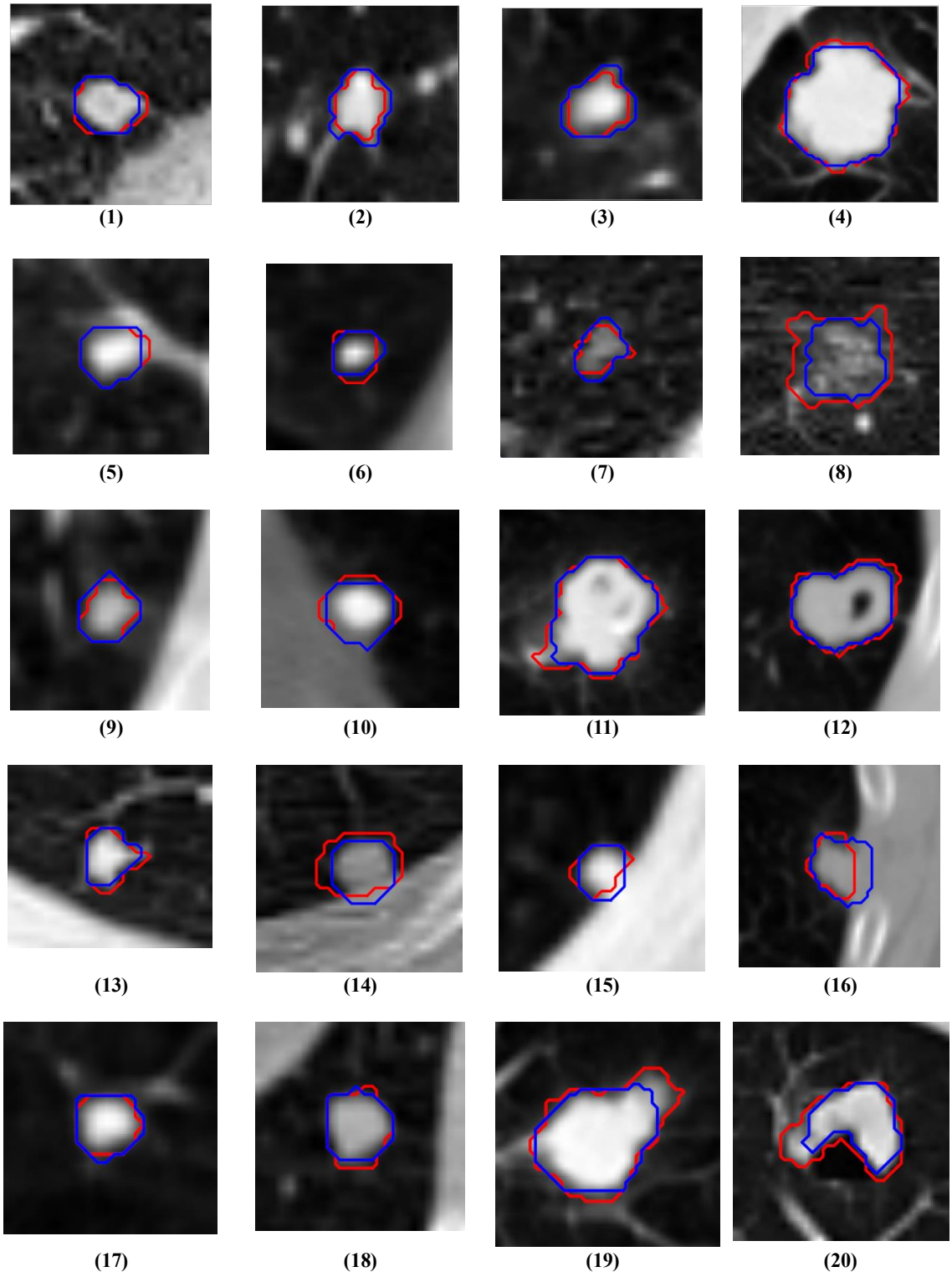

Figure 7. The effectiveness of the proposed method across various contexts.

5. Conclusion

In this paper VLSM algorithm has greatly changed the traditional medical model. Its convenient specimen collection and dynamic detection greatly facilitate the clinic. At present, VLSM can be used for early disease detection, prognosis, recurrence monitoring and personalized cancer treatment. In addition, single-cell sequencing of VLSMs enables the identification of point mutations in oncogenes, reveals the dynamics of genetic mutations in patients undergoing cancer treatment, and predicts drug resistance and phenotypic transformation, ultimately providing a truly personalized approach to medicine. Liquid biopsy and noninvasive

analysis will undoubtedly continue to play an important role in the overall evaluation and treatment of NSCLC patients. However, the results of single-cell gene sequencing of VLSM, that is, the detection of immune markers, are not completely consistent with the results of tissue detection commonly used in clinical practice. There is no unified conclusion on which of the two can better represent the characteristics of the tumor. Further large-sample research is needed, and dynamic monitoring of gene target site mutations and changes in immune markers on VLSM is expected to become an indispensable routine evaluation method in the diagnosis and treatment of NSCLC.

Author contributions

Conceptualization, WJ and LSC; methodology, WJ and LSC; software, WJ and LSC; validation, WJ, AAA and LSC; formal analysis, WJ and LSC; investigation, WJ and LSC; resources, WJ and LSC; data curation, WJ and LSC; writing—original draft preparation, WJ and LSC; writing—review and editing, LSC; visualization, AAA; supervision, LSC; project administration, LSC; funding acquisition, LSC. All authors have read and agreed to the published version of the manuscript.

Conflict of interest

The authors declare no conflict of interest.

References

1. Sung H, Ferlay J, Siegel RL, et al. Global Cancer Statistics 2020: GLOBOCAN Estimates of Incidence and Mortality Worldwide for 36 Cancers in 185 Countries. CA: a Cancer Journal for Clinician 2021; 71(3): 209–249. doi: 10.3322/caac.21660
2. Duan H, Hu JL, Chen ZH, et al. Assessment of circulating tumor DNA in cerebrospinal fluid by whole exome sequencing to detect genomic alterations of glioblastoma. Chinese Medical Journal 2020; 133(12): 1415–1421. doi: 10.1097/CM9.0000000000000843
3. National Lung Screening Trial Research Team. Reduced lung-cancer mortality with low-dose computed tomographic screening. The New England Journal of Medicine 2011; 365(5): 395–409. doi: 10.1056/NEJMoa1102873
4. Schabath MB, Cote ML. Cancer progress and priorities: Lung cancer. Cancer Epidemiology, Biomarkers & Prevention 2019; 28(10): 1563–1579. doi: 10.1158/1055-9965.EPI-19-0221
5. Wu F, Wang L, Zhou C. Lung cancer in China: Current and prospect. Current opinion in oncology 2021; 33(1): 40–46. doi: 10.1097/CCO.0000000000000703
6. Huang M, Wang W. Application observation of expression of serum cytokeratin 19 fragment, neuron-specific enolase, and squamous cell carcinoma antigen in the differential diagnosis of early lung cancer and pulmonary tuberculosis. Chinese Journal of Clinicians 2021; 49(8): 916–919. doi: 10.3969/j.issn.2095-8552.2021.08.011
7. He H, Hu C, Zhong T, et al. The clinical value of combined detection of CEA, NSE, CYFRA21-1, and ProGRP in the diagnosis of lung cancer. Experimental and Laboratory Medicine 2019; 37(3): 435–437. doi: 10.3969/j.issn.1674-1129.2019.03.028
8. Bruzzi JF, Munden RF. PET/CT imaging of lung cancer. Journal of Thoracic Imaging 2006; 21(2): 123–136. doi: 10.1097/00005382-200605000-00004
9. Munden RF, Swisher SS, Stevens CW, Stewart DJ. Imaging of the patient with non-small cell lung cancer. Radiology 2005; 237(3): 803–818. doi: 10.1148/radiol.2373040966
10. Birim Ö, Kappetein AP, Stijnen T, Bogers AJJC. Meta-analysis of positron emission tomographic and computed tomographic imaging in detecting mediastinal lymph node metastases in nonsmall cell lung cancer. The Annals of Thoracic Surgery 2005; 79(1): 375–382. doi: 10.1016/j.athoracsur.2004.06.041
11. Neal RD, Barham A, Bongard E, et al. Immediate chest X-ray for patients at risk of lung cancer presenting in primary care: randomised controlled feasibility trial. British Journal of Cancer 2017; 116(3): 293–302. doi: 10.1038/bjc.2016.414
12. De González AB, Darby S. Risk of cancer from diagnostic X-rays: Estimates for the UK and 14 other countries. The Lancet 2004; 363(9406): 345–351. doi: 10.1016/S0140-6736(04)15433-0
13. Blanchon T, Bréchot J-M, Grenier P A, et al., Baseline results of the Depiscan study: A French randomized pilot trial of lung cancer screening comparing low dose CT scan (LDCT) and chest X-ray (CXR). Lung Cancer 2007; 58(1): 50–58. doi: 10.1016/j.lungcan.2007.05.009
14. Sawka A, Crawford A, Peh CA, Nguyen P. Tracheobronchial calcification on bronchoscopy in a patient with end stage renal failure: An unusual cause of chronic cough. Respirology Case Reports 2019; 7(7): e00456. doi: 10.1002/rcr2.456

15. Ambrosini V, Nicolini S, Caroli P, et al. PET/CT imaging in different types of lung cancer: An overview. European Journal of Radiology 2012; 81(5): 988–1001. doi: 10.1016/j.ejrad.2011.03.020
16. Hochhegger B, Marchiori E, Sedlaczek O, et al. MRI in lung cancer: A pictorial essay. The British Journal of Radiology 2011; 84(1003): 661–668. doi: 10.1259/bjr/24661484
17. Wu NY, Cheng HC, Ko JS, et al. Magnetic resonance imaging for lung cancer detection: experience in a population of more than 10,000 healthy individuals. BMC Cancer 2011; 11: 242. doi: 10.1186/1471-2407-11-242
18. Ohno Y, Koyama H, Lee HY, et al. Magnetic resonance imaging (MRI) and positron emission tomography (PET)/MRI for lung cancer staging. Journal of Thoracic Imaging 2016; 31(4): 215–227. doi: 10.1097/RTI.0000000000000210
19. Chu GCW, Lazare K, Sullivan F. Serum and blood based biomarkers for lung cancer screening: a systematic review. BMC Cancer 2018; 18(1): 181. doi: 10.1186/s12885-018-4024-3
20. Wu Y, Ma W, Gong M, et al. Novel fuzzy active contour model with kernel metric for image segmentation. Applied Soft Computing 2015; 34: 301–311. doi: 10.1016/j.asoc.2015.04.058
21. Li C, Huang R, Ding Z, et al. A level set method for image segmentation in the presence of intensity inhomogeneities with application to MRI. IEEE transactions on image processing 2011; 20(7): 2007–2016. doi: 10.1109/TIP.2011.2146190
22. Liu L, Zhang Q, Wu M, et al. Adaptive segmentation of magnetic resonance images with intensity inhomogeneity using level set method. Magnetic resonance imaging 2013; 31(4): 567–574. doi: 10.1016/j.mri.2012.10.010
23. Liu Y, He C, Wu Y. Variational model with kernel metric-based data term for noisy image segmentation. Digital Signal Processing 2018; 78: 42–55. doi: 10.1016/j.dsp.2018.01.017